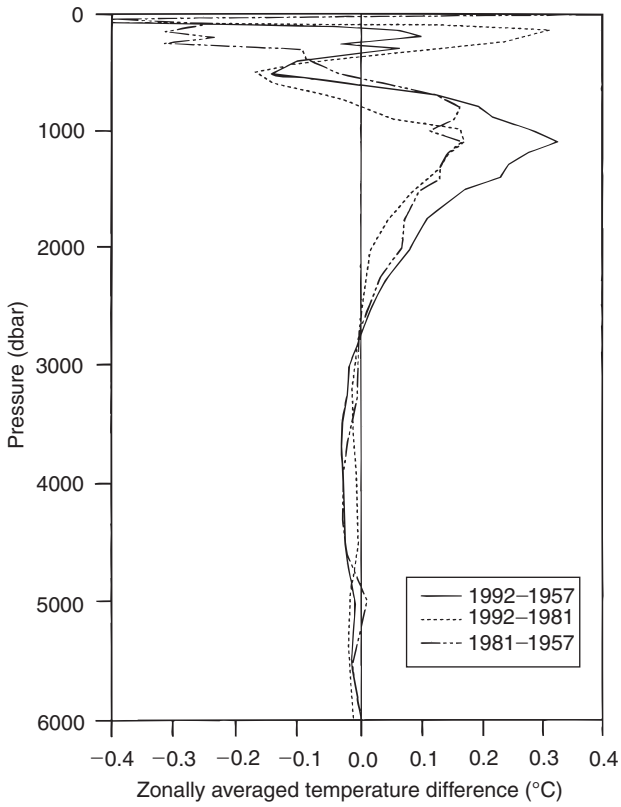

Figure 12 Temperature changes (°C) in the subtropical North Atlantic (24°N), 1957–1992. The measurements have been averaged across 24°N between North Africa and Florida. (Reproduced from Parrilla G, Lavin A, Bryden H, Garcia M and Millard R (1994) Rising temperatures in the subtropical North Atlantic. *Nature* 369: 48–51.)

not as reliable but, nevertheless, changes can be still detected (*see* **Freshwater Transport and Climate**).

Salinity measurements in the Mediterranean over the last century have shown a warming of the Western Mediterranean Deep Water of 0.1°C and increase of 0.05 in salinity. The reasons for this change are not known, but it has been speculated that the change in salinity may be attributed to a reduction in the freshwater flow due to the damming of the Nile and of rivers flowing into the Black Sea.

An important recently identified question is the stability of the thermohaline circulation. The thermohaline circulation is driven by small density differences and therefore changes in the temperature and salinity arising from global warming may alter the thermohaline circulation. In particular, theoretical modeling of the ocean circulation has shown that the thermohaline circulation may be reduced or turned off completely when significant excess fresh water is added to the subpolar ocean. In the event of thermohaline circulation being significantly reduced or stopped, it may take many centuries before it returns to its present value (*see* **Abrupt Climate Change, North Atlantic Oscillation (NAO)**).

In view of the current levels of uncertainty, it is necessary to continue to monitor the ocean circulation, as this will provide the key to the understanding of the present circulation and enhance our ability to predict future changes in circulation.

See also

Abrupt Climate Change. Abyssal Currents. Antarctic Circumpolar Current. Arctic Basin Circulation. CFCs in the Ocean. Current Systems in the Atlantic Ocean. Dispersion and Diffusion in the Deep Ocean. Drifters and Floats. Elemental Distribution: Overview. El Niño Southern Oscillation (ENSO). Florida Current, Gulf Stream and Labrador Current. Flows in Straits and Channels. Freshwater Transport and Climate. General Circulation Models. Heat Transport and Climate. Inverse Models. Moorings. North Atlantic Oscillation (NAO). Regional and Shelf Sea Models. Ships. Thermohaline Circulation. Tritium–Helium Dating. Water Types and Water Masses. Waves on Beaches. Wind Driven Circulation.

Further Reading

Gill AE (1982) *Atmosphere–Ocean Dynamics*. London: Academic Press.

Siedler G, Church J and Gould (2001) *Ocean Circulation and Climate*. London: Academic Press.

Summerhayes CP and Thorpe SA (1996) *Oceanography – An Illustrated Guide*. London: Manson Publishing.

Wells NC (1997) *The Atmosphere and Ocean: A Physical Introduction*, 2nd edn. Chichester: John Wiley.

OCEAN COLOR FROM SATELLITES

C. McClain, NASA Goddard Space Flight Center, Greenbelt, MD, USA

Copyright © 2001 Academic Press

doi:10.1006/rwos.2001.0338

Introduction

The term 'ocean color' refers to the spectral composition of the visible light field that emanates from the ocean. The color of the ocean depends on the

solar irradiance spectra, atmospheric conditions, solar and viewing geometries, and the absorption and scattering properties of water and the substances that are dissolved and suspended in the water column, e.g. phytoplankton and suspended sediments. Water masses whose reflectance is determined primarily by absorption by water and phytoplankton are generally referred to as 'Case 1' waters. In other situations where scattering is the dominant process, or where absorption is dominated by substances other than phytoplankton or their derivatives the term 'Case 2' is applied.

The primary optical variable of interest for remote sensing purposes is the water-leaving radiance, i.e. the subsurface upwelled radiance (light moving upwards in the water column) propagating through the air–sea interface, which does not include the downwelling irradiance (light moving downward through the atmosphere) reflected at the interface. To simplify the interpretation of ocean color, measurements of the water-leaving radiance are normalized by the surface downwelling irradiance to produce reflectance spectra which provide an unambiguous measure of the ocean's subsurface optical signature. Clear open-ocean reflectances have a spectral peak at blue wavelengths because water absorbs strongly in the near-infrared and scatters blue light more effectively than at longer wavelengths. As the concentrations of microscopic green plants (phytoplankton) and suspended materials increase, absorption and scattering reduce the reflectance at blue wavelengths and increase the reflectance at green wavelengths, i.e. the color shifts from blue to green and brown. This spectral shift in reflectance, as amounts of dissolved and suspended constituents increase, can be quantified and used to estimate concentrations of optically active components such as chlorophyll-*a*.

The goal of satellite ocean color analysis is to accurately estimate the water-leaving radiance spectra in order to derive other geophysical quantities from those spectra, e.g. chlorophyll-*a* concentration and diffuse attenuation coefficient. The motivation for spaceborne observations of this kind lies in the need for frequent high-resolution measurements of these geophysical parameters on regional and global scales for addressing both research and operational requirements associated with marine primary production, ecosystem dynamics, fisheries management, ocean dynamics, and coastal sedimentation and pollution, to name a few. The first proof-of-concept satellite ocean color mission was the Coastal Zone Color Scanner (CZCS) on the Nimbus-7 spacecraft which was launched in the summer of 1978. The CZCS was intended to be a 1 year demonstration with very limited data collection, ground processing, and data validation requirements. However, because of the extraordinary quality and unexpected utility of the data for both coastal and open ocean research, data collection continued until June 1986 when the sensor ceased operating. The entire CZCS data set was processed, archived, and released to the research community by 1990. As a result of the CZCS experience, a number of other ocean color missions have been launched, e.g., the Ocean Color and Temperature Sensor (OCTS, Japan, 1996–97), the Sea-viewing Wide Field-of-view Sensor (SeaWiFS, US, 1997 and continuing), and the Moderate Resolution Imaging Spectroradiometer (MODIS, US, 2000 and continuing), with the expectation that continuous global observations will be maintained as part of an operational monitoring program.

Ocean Color Theoretical and Observational Basis

Reflectance can be defined in a number of ways. The most common definition for irradiance reflectance, R, just below the surface is as given in eqn [1].

$$R(\lambda) = \frac{E_{\mathrm{u}}(\lambda, 0^-)}{E_{\mathrm{d}}(\lambda, 0^-)} \qquad [1]$$

E_{u} and E_{d} are the upwelling and downwelling irradiances, respectively, and the superscript minus sign implies the value just beneath the surface. In general, irradiance and radiance are functions of depth (or altitude in the atmosphere) and viewing geometry with respect to the sun. R has been theoretically related to the absorption and scattering properties of the ocean as in eqn [2] where f is a function of solar zenith angle, among other things, and is approximately equal to 0.33, $b_{\mathrm{b}}(\lambda)$ is the backscattering coefficient, and $a(\lambda)$ is the absorption coefficient.

$$R(\lambda) \cong f\frac{b_{\mathrm{b}}(\lambda)}{a(\lambda)} = f\sum_i \frac{b_{\mathrm{b}}^i(\lambda)}{a^i(\lambda)} \qquad [2]$$

Eqn [2] holds where $b_{\mathrm{b}}(\lambda) \ll a(\lambda)$, which is the case for most coastal and open ocean waters. Both $b_{\mathrm{b}}(\lambda)$ and $a(\lambda)$ represent the sum of the contributions of the various optical components (water, inorganic particulates, dissolved substances, phytoplankton, etc.) which are often specified explicitly as indicated in eqn [2]. When concentrations of substances (e.g., chlorophyll-*a*) are measured, the coefficients can be specified in terms of the concentrations, e.g.,

$a_\varphi(\lambda) = a^*_\varphi(\lambda)$[Chl$a$] where $a_\varphi(\lambda)$ and $a^*_\varphi(\lambda)$ are the phytoplankton absorption coefficient and specific absorption coefficient, respectively, and [Chl$a$] is the chlorophyll-a concentration. The absorption coefficients are designated for phytoplankton rather than chlorophyll-a because the actual absorption by living cells can vary substantially for a fixed amount of chlorophyll-a.

The relationship between the upwelling radiance, L_u, and the upwelling irradiance, E_u, just beneath the surface is given by eqn [3].

$$L_u(\lambda,0^-) = \frac{E_u(\lambda,0^-)}{Q} \qquad [3]$$

If the angular distribution of E_u were directionally uniform, i.e. Lambertian, Q would equal π. However, the irradiance distribution is not uniform and is dependent on a number of variables. Some experimental results indicate that Q is roughly 4.5.

For satellite applications, it is more appropriate to use the reflectance just above the surface than $R(\lambda)$. Therefore, remote sensing reflectance, $R_{rs}(\lambda)$, and normalized water-leaving radiance, $L_{wn}(\lambda)$, are commonly used. These are defined as according to eqns [4] and [5].

$$R_{rs}(\lambda) = \frac{L_w(\lambda)}{E_d(\lambda,0^+)} \qquad [4]$$

and

$$L_{wn}(\lambda) = \left(\frac{1-\rho}{n^2}\right)\frac{F_0(\lambda)L_w(\lambda)}{E_d(\lambda,0^+)} \qquad [5]$$

there ρ is the surface Fresnel reflectance, n is the index of refraction, F_0 is the extraterrestrial solar irradiance, L_w is the water-leaving radiance, and the superscript plus sign denotes the value just above the air–sea interface. The term in parenthesis is approximately equal to 0.54. Thus, R_{rs} is proportional to L_{wn}. The water-leaving radiance is the upwelled radiance just above the surface, excluding the light reflected by the surface, i.e., $L_w(\lambda) = L_u(\lambda,0^+)$, and is proportional to the subsurface upwelled radiance (eqn [6]).

$$L_w(\lambda) = 0.54L_u(\lambda,0^-) \qquad [6]$$

Surface reflectance includes the direct component of photons not scattered by the atmosphere, the indirect component from photons that are scattered by the atmosphere (skylight), and the contribution of whitecaps. The angular distribution of surface reflection broadens as wind speed increases and the sea surface roughens. The contribution from whitecaps also increases with wind speed. For clear Case 1 waters, i.e., areas where the chlorophyll-a is less than about 0.25 mg Chl$a$ m^{-3}, the L_{wn} spectrum is fairly constant, e.g., $L_{wn}(550) \approx 0.28$ mW cm^{-2} μm^{-1} sr^{-1} (sr denotes steradians), and the values are referred to as 'clear water normalized water-leaving radiances'.

The other optical parameter of interest is the diffuse attenuation coefficient for upwelled radiance, K_{Lu}, (eqn [7]).

$$K_{Lu}(\lambda,z) = -\frac{1}{L_u(\lambda,z)}\frac{dL_u(\lambda,z)}{dz} \qquad [7]$$

Near the surface where optical constituents are relatively uniform, eqn [8] is used.

$$L_u(\lambda,z) = L_u(\lambda,0)e^{-K_{Lu}(\lambda)z} \qquad [8]$$

Similar K relationships hold for irradiance. For convenience, $K(\lambda)$ will be used to denote $K_{Lu}(\lambda)$. The various upwelling and downwelling diffuse attenuation coefficients for radiance and irradiance are commonly interchanged, but strictly speaking they are different quantities and are not equal.

Key to the ocean color measurement technique are the relationships between the solar irradiance, water absorption, and chlorophyll-a absorption spectra, chlorophyll-a being the primary chemical associated with photosynthesis. The solar spectrum peaks at blue wavelengths which correspond to the maximum transparency of water and the peak in chlorophyll-a absorption. Thus, phytoplankton photosynthesis is tuned to the spectral range of maximum light. **Figure 1** provides spectra for $F_0(\lambda)$, $a^*_\varphi(\lambda)$, and ocean water absorption ($a_w(\lambda)$). There are other important substances besides chlorophyll-a such as yellow substance (also known as gelbstoff, gilvin, and color dissolved organic matter) which may be inferred from ocean color, but the focus here will be on chlorophyll-a.

Satellite Ocean Color Methodology

In order to obtain accurate estimates of geophysical quantities such as chlorophyll-a and $K(490)$ from satellite measurements, a number of radiometric issues must be addressed including (1) sensor design and performance, (2) post-launch sensor calibration stability, (3) atmospheric correction, i.e., the removal of light due to atmospheric scattering, atmospheric absorption, and surface reflection, and (4)

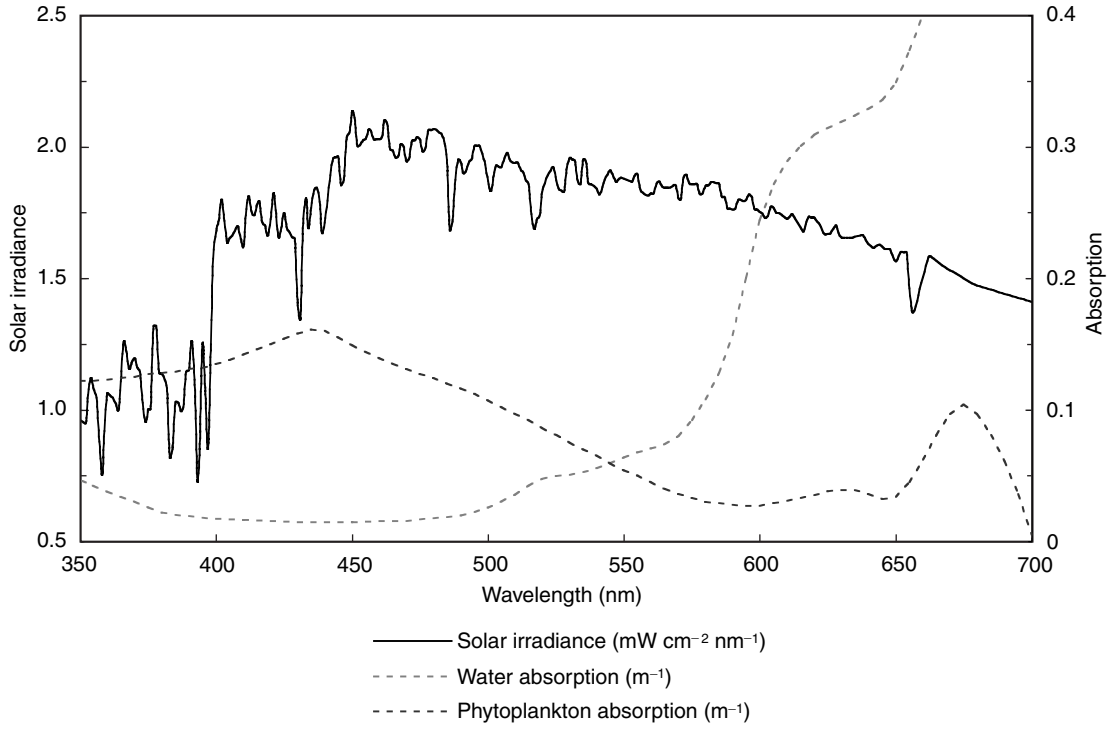

Figure 1 Solar irradiance, chlorophyll-specific absorption, and water absorption spectra.

bio-optical algorithms, i.e., the transformation of $R_{rs}(\lambda)$ or $L_{wn}(\lambda)$ values into geophysical parameter values. Items (2)–(4) represent developments that progress over time during a mission. For example, over the first 2 years of operation, the radiometric sensitivity of SeaWiFS degraded by as much as 8% in one of the bands. Also, as radiative transfer theory develops and additional optical data are obtained, atmospheric correction and bio-optical algorithms will improve and replace previous versions, and new data products will be defined by the research community. Therefore, flight projects, such as SeaWiFS, are prepared to periodically reprocess their entire data set. **Figure 2** provides a graphical depiction of all components of the satellite measurement scenario, each aspect of which is discussed below.

Sensor Design and Performance

Sensor design and performance characteristics encompass many considerations that cannot be elaborated on here, but are essential to meeting the overall measurement accuracy requirements. Radiometric factors include wavelength selection, bandwidth, saturation radiances, signal-to-noise ratios, polarization sensitivity, temperature sensitivity, scan angle dependences (scan modulation), stray-light rejection, out-of-band contamination, field-of-view (spatial resolution), band co-registration, and a number of others, all of which must be accurately quantified (characterized) prior to launch and incorporated into the data-processing algorithms. Other design features may include sensor tilting for sunglint avoidance and capacities for tracking the sensor stability on-orbit (e.g., internal lamps, solar diffusers and lunar views), as instruments generally lose sensitivity over time due to contamination of optical components, filter degradation, etc. Also, there are a variety of spacecraft design criteria including attitude control for accurate navigation, power (solar panel and battery capacities), onboard data storage capacity, telemetry bandwidth (command uplink and downlink data volumes, transmission frequencies, and ground station compatibility and contact constraints), and realtime data broadcast (high resolution picture transmission, HRPT, station compatibility). Depending on the specifications, instruments can be built in a variety of ways to optimize performance. For example, the Coastal Zone Color Scanner used a grating for spectral separation while SeaWiFS uses filters. **Table 1** provides a summary of past, present, and planned ocean color sensors and their performance specifications. It is important to note that only the two MODIS instruments have a common design.

To date, all ocean color missions, both previous and currently approved, have been designed for low-altitude sun-synchronous orbits, although

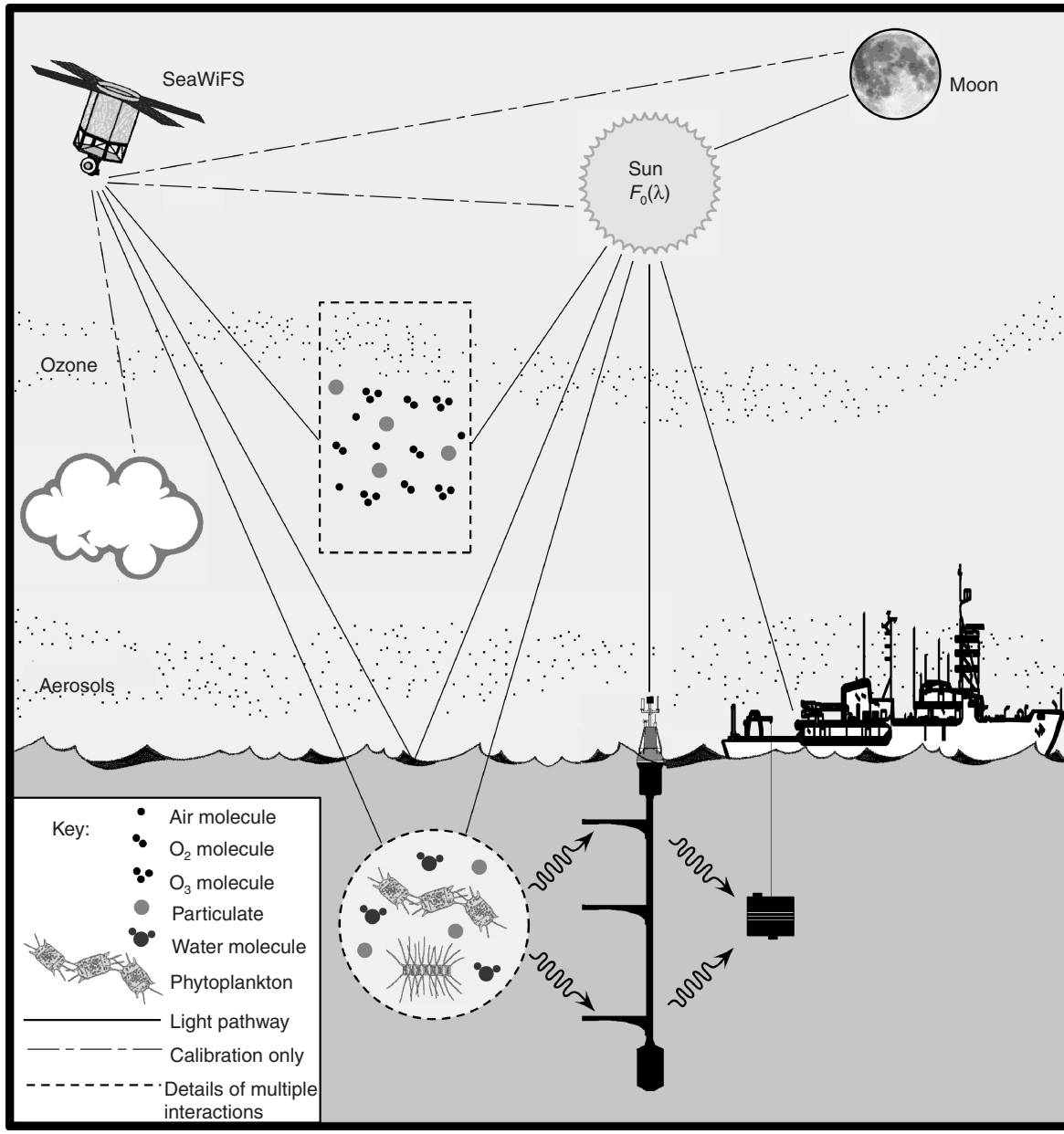

Figure 2 Depiction of the various sensor, atmospheric, and oceanic optical processes which must be accurately accounted for in satellite ocean color data processing.

sensors on high-altitude geostationary platforms are being considered. Sun-synchronous orbits provide global coverage as the orbit advances westward, keeping pace with the sun, so the data are collected at about the same local time each day, e.g., local noon. Multiple views for a given day are possible only at high latitudes where the orbit tracks converge. **Figure 3** shows the daily global area coverage (GAC) of SeaWiFS. The gaps between the swaths are filled on the following day as the ground track pattern progressively shifts. The SeaWiFS local area coverage (LAC) extends the swath to greater scan angles, but at large scan angles, pixels (the area on the surface being viewed) become much larger and the atmospheric corrections are less reliable, so these data are not included in the operational processing. The data gaps in each swath about the subsolar point are where the sensor is tilted from -20° to $+20^\circ$ to avoid viewing into the sunglint. The tilt operation is staggered on successive days in order to ensure every-other-day coverage of the gap. Geostationary orbits, i.e., orbits having a fixed subsatellite (nadir) point on the equator, only allow hemispheric coverage with decreased spatial

Table 1 Summary of satellite ocean color sensor and orbit characteristics

Mission instrument (*launch*)	*Visible bands* (*nm*)	*Resolution* (*km*)	*Swath (km)*	*Tilt* (°)	*Onboard calibration*	*Orbit node* (*inclination*)
Nimbus-7 CZCS (1978)	443, 520, 550, 670, 750 11.5 μm	0.8	1600	0 ± 20	Internal lamps	12:00 noon ascending
ADEOS-I OCTS (1996)	412, 443, 490, 520, 565, 670, 765, 865	0.7	1400	0 ± 20	Solar Internal lamps	10:30 descending
ADEOS-I POLDER (1996)	443, 490, 565, 670, 763, 765, 865, 910	6.2	2471	N/A	None	10:30 descending
Orbview-2 SeaWiFS (1997)	412, 443, 490, 510, 555, 670, 765, 865	1.1 (LAC) 4.5 (GAC)	2800 (LAC) 1500 (GAC)	0 ± 20	Solar diffuser Lunar imaging	12:00 noon descending
EOS MODIS (Terra-2000) (Aqua-2001)	412, 443, 488, 531, 551, 667, 678, 748, 869	1.0	1500	None	Solar diffuser (with stability monitor) Spectral Radiometric Calibration Assembly	10:30 descending 1:30 ascending
ENVISAT-1 MERIS (2001)	412, 443, 490, 510, 560, 620, 665, 681, 709, 754, 760, 779, 870, 890, 900	0.3 (LAC) 1.2 (GAC)	1150	None	Solar diffusers (3)	10:30 descending
ADEOS-II GLI (2001)	400, 412, 443, 460, 490, 520, 545, 565, 625, 666, 680, 710, 749, 865	1.0	1600	0 ± 20	Solar diffuser Internal lamps	10:30 descending

Some sensors have more channels than are indicated which are used for other applications. There are a number of other ocean color missions not listed because the missions are not designed to routinely generate global data sets.

resolution away from nadir, but can provide multiple views each day. Multiple views per day allow for the evaluation of tidal and other diurnal time-dependent biases in sampling to be evaluated, and also provide more complete sampling of a given location as cloud patterns change.

Post-launch Sensor Calibration Stability

The CZCS sensitivity at 443 nm changed by about 50% during its 7.7 years of operation. Even the relatively small changes noted above for SeaWiFS undermine the mission objectives for global change research because they introduce spurious trends in the derived products. Quantifying changes in the sensor can be very difficult, especially if the changes are gradual. In the case of the CZCS, there was no on-going comprehensive validation program after its first year of operation, because the mission was a proof-of-concept. As a result, subsequent missions have some level of continuous validation. In the case of SeaWiFS, a combination of solar, lunar, and field observations (oceanic and atmospheric) are used. The solar measurements are made daily using a solar diffuser to detect sudden changes in the sensor. The solar measurements cannot be used as an absolute calibration because the diffuser reflectance gradually changes over time. Lunar measurements are made once a month at a fixed lunar phase angle and provide an accurate estimate of the sensor stability relative to the first lunar measurement. The lunar measurements cannot be used for an absolute calibration because the moon's surface reflectance is not known to a sufficient accuracy. Time-series of the water-leaving radiance from uniform clear-water regions can be used to track trends in the satellite retrievals. For example, the Marine Optical Buoy (MOBY) located off Lanai, Hawaii is being used operationally by the SeaWiFS and MODIS projects. Given cloud cover and satellite sampling frequency at Hawaii, a clear-sky comparison between SeaWiFS and MOBY is achieved about once per week. Typically, the comparisons are noisy and require a long time-series to detect a trend. The lunar data provide a much more detailed history. However, the MOBY

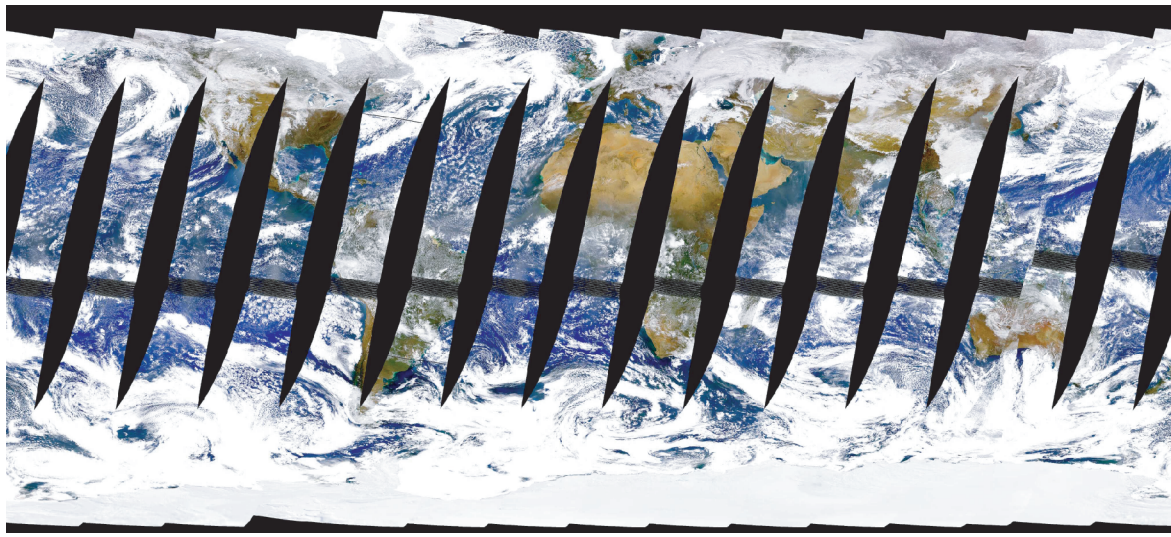

Figure 3 An example of the daily global area coverage (GAC) from SeaWiFS. The SeaWiFS scan extends to $\pm 57^{\circ}$ and samples at about a 1 km resolution. These data are the local area coverage (LAC) and are continuously broadcast for high resolution picture transmission (HRPT) station reception. The GAC data is subsampled at every fourth pixel and line over only the center $\pm 45^{\circ}$ of the scan. GAC data are stored on the spacecraft and downlinked to the NASA and Orbimage Corporation ground stations twice per day.

data allow for the prelaunch calibration of the visible bands to be adjusted so that the mean differences between the observations and the satellite L_w retrievals are minimized. This adjustment is necessary because the prelaunch calibration is only accurate to within about 3%, the sensor can change during launch and orbit-raising, and any biases in the atmospheric correction can be removed in this way. However, in-water measurements cannot help in accessing biases in the near-infrared calibrations. Atmospheric measurements of optical depth and other parameters are needed to evaluate these wavelengths. High altitude top-of-the-atmosphere aircraft measurements offer the possibility of direct comparisons with the satellite, but these are also subject to the same limitations in laboratory calibration accuracy and require many flights to obtain a statistically significant number of comparisons.

Atmospheric Correction

Solar irradiance propagates through the atmosphere, where it is attenuated by molecular (Rayleigh) and aerosol scattering and absorption. Rayleigh scattering can be calculated theoretically with a high degree of accuracy. Aerosol scattering and absorption are much more difficult to estimate because their horizontal and vertical distributions are highly variable, as are their absorption and scattering properties. The estimation of the aerosol effects on the upwelling radiance at the top of the atmosphere is one of the most difficult aspects of satellite remote sensing. Ozone is the primary absorbing gas that must be considered. Fortunately, ozone is concentrated in a thin band near the top of the atmosphere and its global distribution is mapped daily by the Total Ozone Mapping Spectrometer (TOMS) and the Total Ozone Vertical Sounder (TOVS) instruments which are on separate spacecraft. Continuous global satellite ozone measurements have been made since 1978 (TOMS was also an instrument on Nimbus-7), because the ozone layer modulates the amount of ultraviolet radiance reaching the surface. The other absorbing gas of interest is oxygen, which has a strong absorption band (A-band) between 750 and 770 nm. Light that reaches the surface is either reflected or penetrates through the air–sea interface. Simple reflection at a flat interface is called Fresnel reflection and is easily computed theoretically. However, if the surface is wind-roughened or includes foam (whitecaps), then the estimation of the reflected light is more complex and empirical relationships must be invoked. Only a small percentage of the light that enters the water column is reflected upward back through the air–sea interface in the general direction of the satellite sensor. Of that light, only a fraction makes its way back through the atmosphere into the sensor. Each process must be accounted for in estimating the water-leaving radiances. The radiances associated with each process are additive, to the first order, and can be expressed as in eqn [9], where the subscripts denote

total (t), Rayleigh (r), aerosol (a), Rayleigh-aerosol interaction (ra), sun glint (g), and foam (f).

$$L_t(\lambda) = L_r(\lambda) + L_a(\lambda) + L_{ra}(\lambda) + T(\lambda)L_g(\lambda) + t(\lambda)[(L_f(\lambda) + L_w(\lambda))] \quad [9]$$

$T(\lambda)$ is the direct transmittance and $t(\lambda)$ is the diffuse transmittance. L_t is the total radiance observed by the spaceborne sensor and depends only on the sensor calibration. The Rayleigh radiances can be estimated theoretically and the aerosol radiances are usually inferred from near-infrared wavelengths, where L_w is assumed to be negligible. Determining values for all terms on the right side of eqn [9], with the exception of L_w, constitutes the 'atmospheric correction' which allows eqn [9] to be solved for L_w. As mentioned earlier, if L_w is known, then L_t can be adjusted to balance eqn [9] to derive a 'vicarious' calibration of the visible bands.

Bio-optical Algorithms

Bio-optical algorithms are used to define relationships between the water-leaving radiances or reflectances and constituents in the water. These can be strictly empirical (statistical regressions) or semi-empirical relationships, i.e., based on theoretical expressions using measured values of certain optical variables. For example, the empirical chlorophyll-*a* relationship used early in the SeaWiFS mission is depicted in **Figure 4** and is expressed as eqn [10], where $R = \log_{10}[R_{rs}(490)/R_{rs}(555)]$ and [Chl*a*] is chlorophyll-*a* concentration.

$$[\text{Chl}a] = 10^{0.2974 - 2.2429R + 0.8358R^2 - 0.0077R^3} - 0.0929 \quad [10]$$

This relationship was based on observed R_{rs} and chlorophyll-*a* data from many locations and, therefore, was not optimized to a particular biological or optical regime, i.e., a bio-optical province. A similar

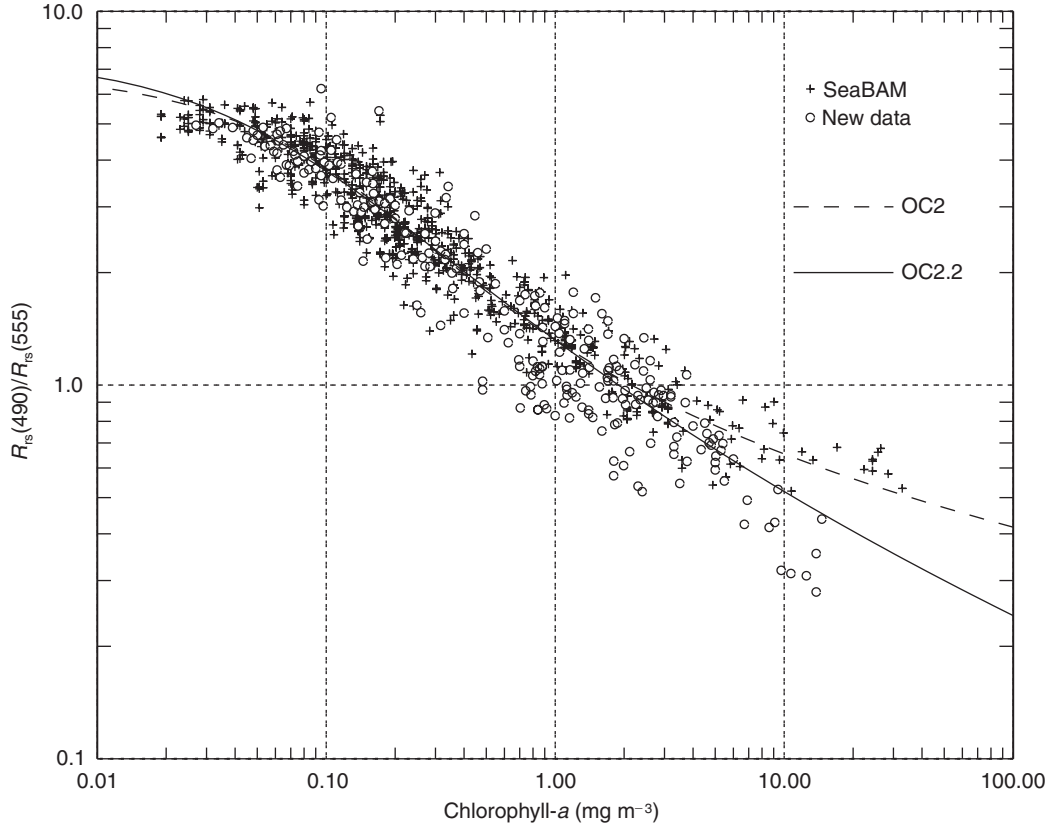

Figure 4 An empirical chlorophyll-*a* algorithm based on a regression of *in situ* chlorophyll-*a* versus $R_{rs}(490)/R_{rs}(555)$ observations. The two curves show the evolution of the algorithm as additional data were incorporated. The OC2 algorithm was based on the SeaWiFS Bio-optical Algorithm Miniworkshop (SeaBAM) data set and was used in the initial SeaWiFS processing. Additional 'New data' were incorporated into the SeaBAM data set resulting in the OC2.2 algorithm which was used in a subsequent reprocessing of the SeaWiFS data set. This change in the algorithm underscores the need for occasionally reprocessing an entire satellite data set as new data and algorithms become available.

relationship holds for $K(490)$ (eqn [11]; the units are m^{-1}).

$$K(490) = 0.016 + 0.156\left(\frac{L_w(490)}{L_w(555)}\right)^{-1.54} \quad [11]$$

Product Validation

Validation of the derived products can be approached in several ways. The most straightforward approach is to compare simultaneous field and satellite data. Another approach is to make statistical comparisons, e.g., frequency distributions, of large *in situ* and satellite data sets. Simultaneous comparisons can provide accurate error estimates, but typically 5% of the observations result in valid matchups mainly because of cloud cover and time differences. **Figure 5** represents all Case 1 (nonturbid) water comparisons for the first 30 months of SeaWiFS. Statistical comparisons of cumulative data

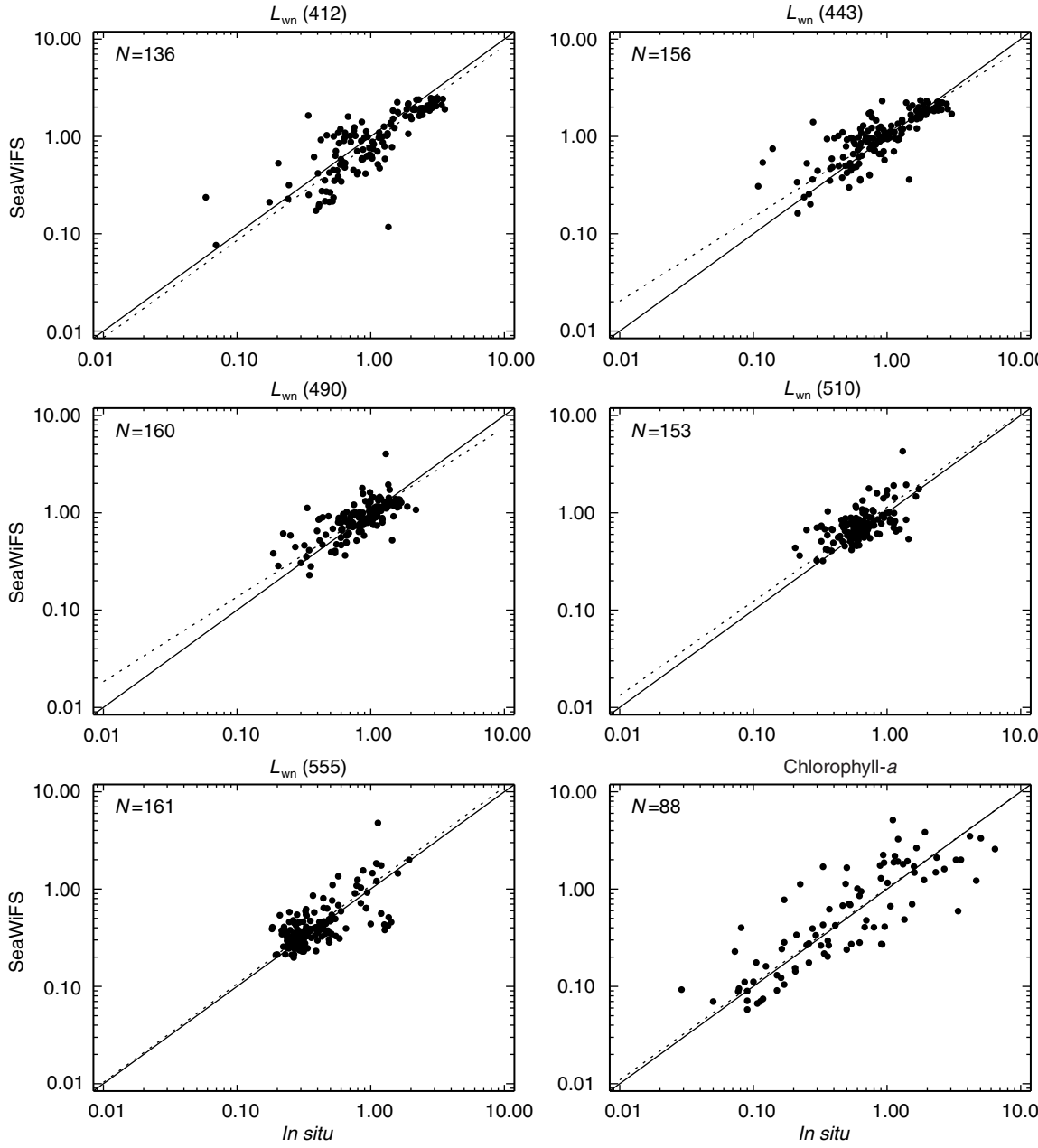

Figure 5 A comparison of simultaneous SeaWiFS-derived and *in situ* L_{wn} and chlorophyll-*a* data. Only about 2% of the field data collected are used in the comparisons, because many of the data are excluded due to cloud cover, time difference, and other rejection criteria. The dashed line is the least-squares fit to the data and *N* is the number of comparisons.

sets allow utilization of much more data, but can be subject to sampling biases. Differences in field measurements and satellite estimates can be due to a number of sources including erroneous satellite estimations of L_w, inaccurate *in situ* values, and an inappropriate algorithm. To minimize *in situ* measurement errors, the SeaWiFS project initiated a calibration comparison program, the development and documentation of *in situ* measurement protocols, and a number of technology development activities.

Because missions overlap in time and the overall goal of the international science community and the space agencies is to develop a time-series of global observations spanning several decades for global change research, the Sensor Intercomparison and Merger for Biological and Interdisciplinary Oceanic Studies (SIMBIOS) was initiated by the National Aeronautics and Space Administration (NASA) in 1997. The purpose of the SIMBIOS program is to promote cross-calibration of spaceborne sensors, compatibility in data products, and consistency in data quality so that (1) simultaneous data sets can be combined for more complete global coverage and (2) the global time-series developed by piecing together observations from numerous missions over time will be free of calibration drift and processing artifacts which can produce time-series trends that are not geophysical. The SIMBIOS program includes a Project Office and a science team selected under NASA Research Announcements. The program has greatly increased the amount of *in situ* marine optical and pigment data and coastal atmospheric optical data available for algorithm development and product validation. The Project Office works closely with the International Ocean Color Coordinating Group (IOCCG) and other space agencies.

Satellite Ocean Color Data Sets and Applications

In this section, examples of satellite ocean color data products are presented to illustrate some research applications.. These include (1) an annual seasonal cycle of global chlorophyll-*a*, (2) interannual variability due to the El Niño-Southern Oscillation (ENSO) cycle in the equatorial Pacific, (3) mesoscale variability (scenes from the Galapagos Islands), and (4) blooms of special phytoplankton groups (coccolithophores).

Plant growth in the ocean is regulated by the supply of macronutrients such as nitrate and silicate, micronutrients (iron in particular), light, and temperature. Light is modulated by cloud cover and time of year (solar zenith angle). Nutrient supply and temperature are determined by ocean circulation and mixing, especially the vertical fluxes, and heat exchange with the atmosphere. **Figure 6** provides seasonal average chlorophyll-*a* concentrations derived from SeaWiFS. Areas such as the North Atlantic show a clear seasonal cycle. The seasonality in the North Atlantic is the result of deep mixing in the winter which renews the surface nutrient supply because the deeper waters are a reservoir for nitrate and other macronutrients. Once illumination begins to increase in the spring, the mixed layer shallows to provide a well-lit, nutrient-rich surface layer ideal for phytoplankton growth. A bloom results and persists into the summer until zooplankton grazing and nutrient depletion curtail the bloom.

Figure 7 depicts the effects of El Niño and La Niña on the ecosystems of the equatorial Pacific during 1997–98. Under normal conditions, the eastern equatorial Pacific is one of the most biologically productive regions in the world ocean, as westward winds force a divergent surface flow resulting in upwelling of nutrient-rich subsurface water into the euphotic zone, i.e., the shallow illuminated layer where plant photosynthesis occurs. During El Niño, warm nutrient-poor water migrates eastward from the western Pacific and replaces the nutrient-rich water, resulting in a collapse of the ecosystem. Eventually, the ocean–atmosphere system swings back to cooler conditions, usually to colder than normal ocean temperatures, causing La Niña. The result is an extensive bloom which eventually declines to more typical concentrations as the atmosphere–ocean system returns to a more normal state.

The 1998 transition from El Niño to La Niña occurred very rapidly. **Figure 8** compares the chlorophyll-*a* concentrations around the Galapagos Islands in early and late May. During the time between these two high-resolution scenes, ocean temperatures around the islands dropped by about 10°C. The chlorophyll-*a* concentrations jumped dramatically as nutrient-rich waters returned and phytoplankton populations could grow unabated in the absence of zooplankton grazers.

The final example illustrates that some phytoplankton have special optical properties which allow them to be uniquely identified. **Figure 9**, a composite of three Rayleigh-corrected SeaWiFS bands, shows an extensive bloom of coccolithophores in the Bering Sea. In their mature stage of development, coccolithophores shed carbonate platelets which turn the water a milky white.

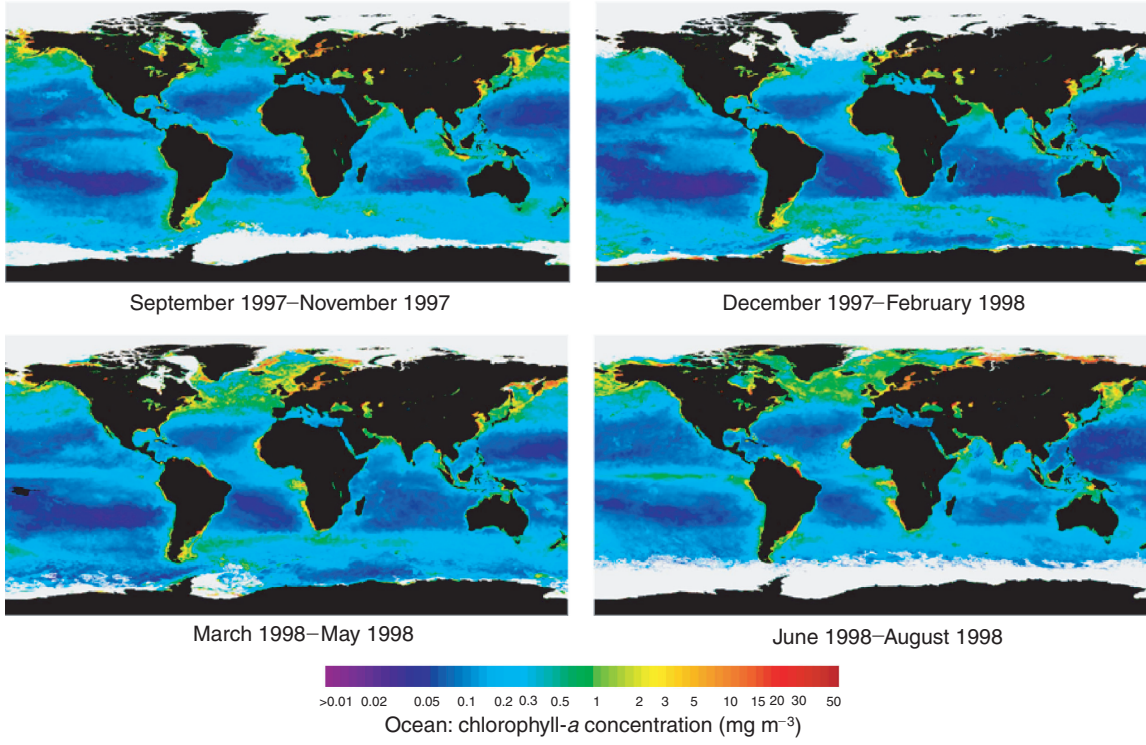

Figure 6 Seasonal average chlorophyll-*a* concentrations from the first year of SeaWiFS operation. The composites combine all chlorophyll-*a* estimates within 9 km square 'bins' obtained during each 3 month period. A variety of quality control exclusion criteria is applied before a sample (pixel) value is included in the average.

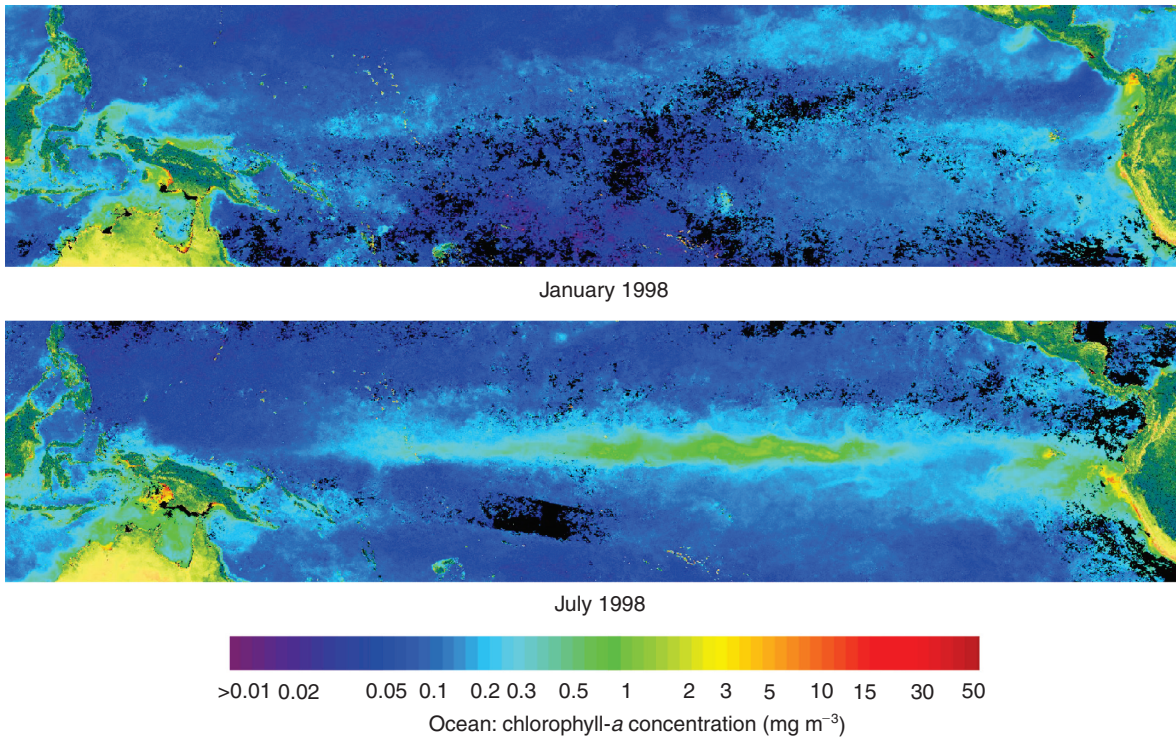

Figure 7 A comparison of the monthly average chlorophyll-*a* concentrations at the peaks of the 1997 El Niño and the 1998 La Niña in the equatorial Pacific Ocean.

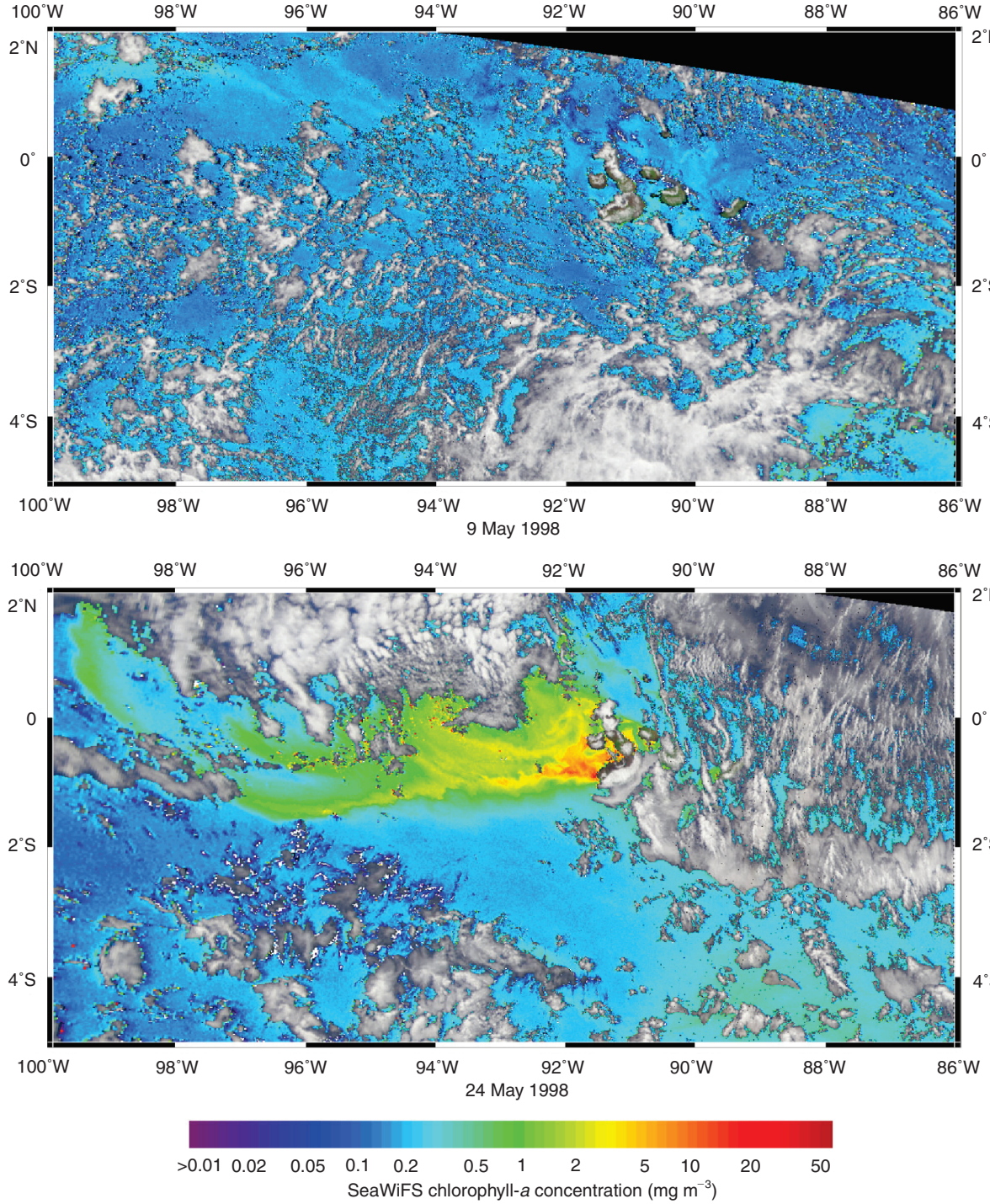

Figure 8 Mesoscale temporal and spatial chlorophyll-*a* variability around the Galapagos Islands in the eastern equatorial Pacific Ocean before and after the sudden onset of the 1998 La Niña. The sea surface temperature near the islands dropped nearly 10°C between May 9 and May 24.

Under these conditions, algorithms for reflectance (eqn [2]) and chlorophyll-*a* concentration (eqn [10]) are not valid. However, the anomalously high reflectance allows for their detection and removal from spatial and temporal averages of the satellite-derived products. Since coccolithophores are of interest for a number of ecological and biogeochemical purposes, satellite ocean color data can be used to map the temporal and spatial distribution of these blooms. In the case of the Bering Sea, the occurrence

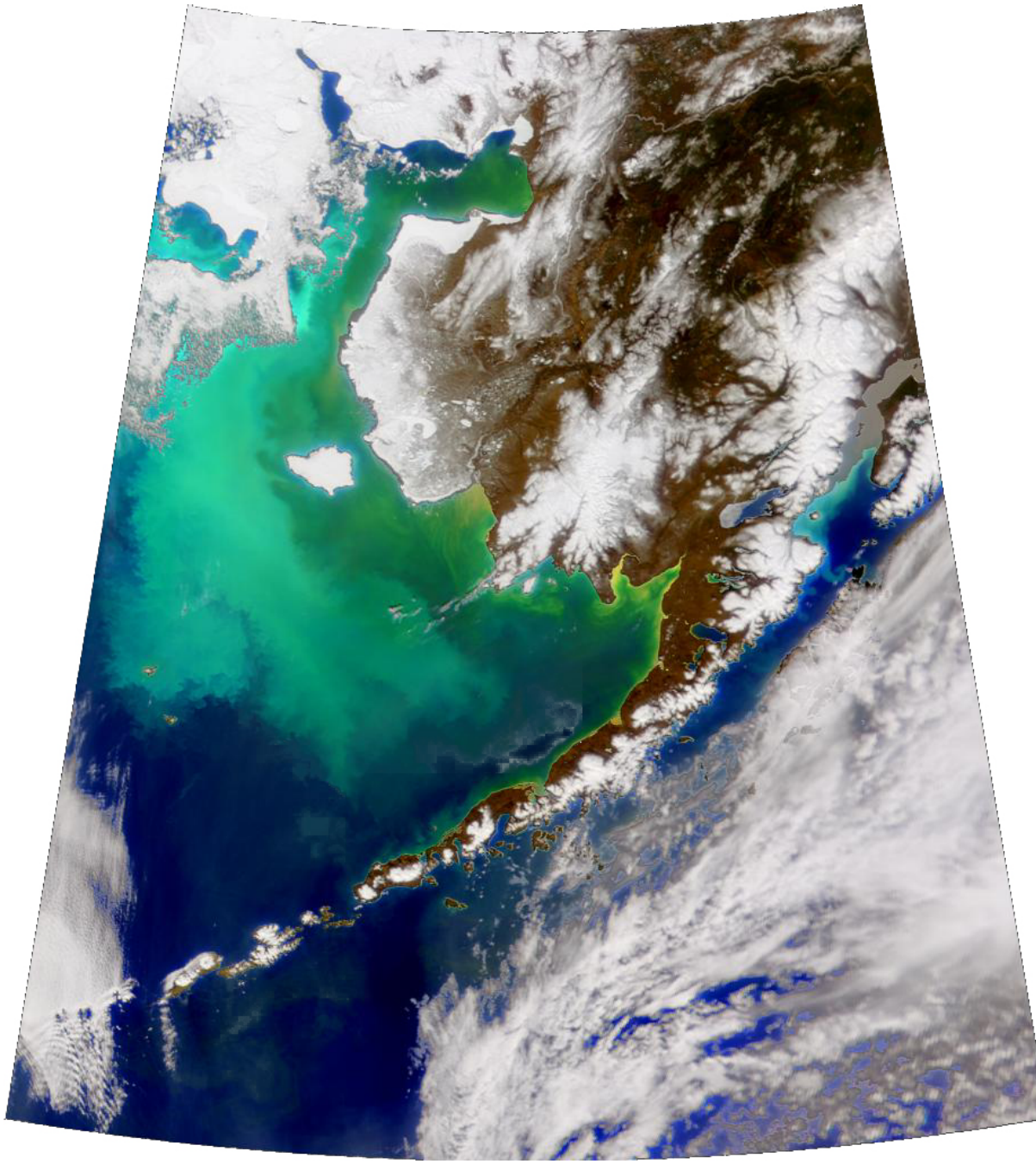

Figure 9 A true color depiction of a coccolithophore, *Emiliania huxleyi*, bloom in the Bering Sea. The true color composite is formed by summing the Rayleigh radiance-corrected 412 nm, 555 nm, and 670 nm SeaWiFS images.

of coccolithophores had not been documented prior to 1997, when the bloom persisted for about 6 months. The ecological impact of the blooms in 1997 and 1998, which encompassed the entire western Alaska continental shelf, was dramatic and may have contributed to extensive starvation of marine mammals and seabirds and prevented salmon from spawning in the rivers along that coast. Research is presently being conducted on methods of identifying other types of blooms such as trichodesmium, important for understanding nitrification in the ocean, and red tides (toxic algal blooms).

Conclusions

Satellite ocean color remote sensing combines a broad spectrum of science and technology. In many ways, the CZCS demonstrated that the

technique could work. However, to advance the state of the art to a degree of sophistication and accuracy required for global change research, many improvements in satellite sensor technology, atmospheric and oceanic radiative transfer modeling, field observation methodologies, calibration metrology, and other areas have been necessary and are continuing to evolve. As these develop, new products and applications will become feasible. It is the intention of the international ocean science community, working with the various space agencies, to develop a continuous long-term global-time series of highly accurate and well-documented satellite ocean color observations which will enable periodic reprocessing of the time series and an unambiguous interpretation of the results.

See also

Aircraft Remote Sensing. Bio-optical Models. Carbon Cycle. El Niño Southern Oscillation (ENSO). Inherent Optical Properties and Irradiance. Iron Fertilization. Large Marine Ecosystems. Ocean Color from Satellites. Ocean Gyre Ecosystems. Pacific Ocean Equatorial Currents. Patch Dynamics. Pelagic Biogeography. Penetrating Shortwave Radiation. Phytoplankton Blooms. Plankton and Climate. Radiative Transfer in the Ocean. Satellite Oceanography, History and Introductory Concepts. Satellite Remote Sensing of Sea Surface Temperatures. Upper Ocean Time and Space Variability. Upwelling Ecosystems.

Further Reading

Barale V and Schlittenhardt PM (1993) *Ocean Colour: Theory and Applications in a Decade of CZCS Experience*. Dordrecht: Kluwer Academic Publishers.

Gordon HR and Morel A (1983) *Remote Assessment of Ocean Color for Interpretation of Satellite Visible Imagery, A Review*. New York: Springer-Verlag.

Jerlov NG and Steeman Nielsen E (1974) *Optical Aspects of Oceanography*. New York: Academic Press.

Jerlov NG (1976) *Marine Optics*. New York: Elsevier Scientific Publishing

Kirk JTO (1994) *Light and Photosynthesis in Aquatic Ecosystems*. Cambridge: Cambridge University Press.

McClain CR and Fargion GS 1999 *SIMBIOS Project 1999 Annual Report*, NASA Technical Memorandum 1999-209486. Greenbelt, MD: NASA Goddard Space Flight Center.

Mobley CD (1994) *Light and Water, Radiative Transfer in Natural Waters*. San Diego: Academic Press.

Robinson IS (1985) *Satellite Oceanography*. Chichester: John Wiley and Sons.

Hooker SB and Firestone ER (eds) *SeaWiFS Technical Report Series*, NASA Technical Memorandum 104566, vols 1–43. Greenbelt, MD: NASA Goddard Space Flight Center.

Hooker SB and Firestone ER (eds) *SeaWiFS Postlaunch Technical Report Series*, NASA Technical Memorandum year-206892, vol. 1–ongoing. Greenbelt, MD: NASA Goddard Space Flight Center.

Shifrin KS (1988) *Physical Optics of Ocean Water*. New York: American Institute of Physics.

Stewart RH (1985) *Methods of Satellite Oceanography*. Los Angeles: University of California Press.

OCEAN GYRE ECOSYSTEMS

M. P. Seki and J. J. Polovina,
National Marine Fisheries Service, Honolulu, HI, USA

Copyright © 2001 Academic Press

doi:10.1006/rwos.2001.0296

The Generalized Open-Ocean Food Web

Food webs, simply put, describe all of the trophic relationships and energy flow between and among the component species of a community or ecosystem. A food chain depicts a single pathway up the food web. The first trophic level of a simple food chain in the open ocean begins with the phytoplankton, the autotrophic primary producers, which build organic materials from inorganic elements. Herbivorous zooplankton that feed directly on the phytoplankton are the primary consumers and make up the second trophic level. Subsequent trophic levels are formed by the carnivorous species of zooplankton that feed on herbivorous species and by the carnivores that feed on smaller carnivores, and so on up to the highest trophic level occupied by those adult animals that have no predators of their own other than humans; these top-level predators may include sharks, fish, squid, and mammals.

In ocean gyres, the dominant phytoplankton, especially in oligotrophic waters, are composed of very small forms, marine protozoans such as zooflagellates and ciliates become important intermediary links, and the food chain is lengthened. There are thus typically about five or six trophic levels in these ecosystems. In contrast, large diatoms dominate in nutrient-rich upwelling regions, resulting in shorter food chains of three or four trophic levels since large zooplankton or fish can feed directly on